# Assessing the *In Vivo* Targeting Efficiency of Multifunctional Nanoconstructs Bearing Antibody-Derived Ligands

Luisa Fiandra,[‡] Serena Mazzucchelli,[‡] Clara De Palma,[‡] Miriam Colombo,[†,§] Raffaele Allevi,[†] Silvia Sommaruga,[‡] Emilio Clementi,[†,||] Michela Bellini,[§] Davide Prosperi,[§,⊥,]* and Fabio Corsi[†,‡,]*

[†]Dipartimento di Scienze Biomediche e Cliniche "Luigi Sacco", Università di Milano, via G.B. Grassi 74, 20157 Milano, Italy, [‡]Ospedale L. Sacco, via G.B. Grassi 74, 20157 Milano, Italy, [§]NanoBioLab, Dipartimento di Biotecnologie e Bioscienze, Università di Milano-Bicocca, piazza della Scienza 2, 20126 Milano, Italy, [⊥]Laboratorio di Biofisica e Nanomedicina, Polo Tecnologico, Fondazione Don Gnocchi IRCCS-ONLUS, 20148 Milano, Italy, and [||]Istituto Scientifico Eugenio Medea, 23842 Bosisio Parini, Italy

ABSTRACT A great challenge in nanodiagnostics is the identification of new strategies aimed to optimize the detection of primary breast cancer and metastases by the employment of target-specific nanodevices. At present, controversial proof has been provided on the actual importance of surface functionalization of nanoparticles to improve their *in vivo* localization at the tumor. In the present paper, we have designed and developed a set of multifunctional nanoprobes, modified with three different variants of a model antibody, that is, the humanized monocolonal antibody trastuzumab (TZ), able to selectively target the HER2 receptor in breast cancer cells. Assuming that nanoparticle accumulation in target cells is strictly related to their physicochemical properties, we performed a comparative study of internalization, trafficking, and metabolism in MCF7 cells of multifunctional nanoparticles (MNP) functionalized with TZ or with alternative lower molecular weight variants of the monoclonal antibody, such as the half-chain (HC) and scFv fragments (scFv). Hence, to estimate to what extent the structure of the surface bioligand affects the targeting efficiency of the nanoconjugate, three cognate nanoconstructs were designed, in which only the antibody form was differentiated while the nanoparticle core was maintained unvaried, consisting of an iron oxide spherical nanocrystal coated with an amphiphilic polymer shell. *In vitro*, *in vivo*, and *ex vivo* analyses of the targeting efficiency and of the intracellular fate of MNP-TZ, MNP-HC, and MNP-scFv suggested that the highly stable MNP-HC is the best candidate for application in breast cancer detection. Our results provided evidence that, in this case, active targeting plays an important role in determining the biological activity of the nanoconstruct.
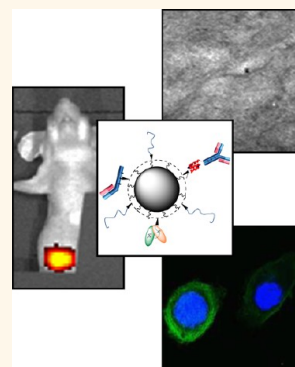
KEYWORDS: magnetic nanoparticles · active targeting · breast cancer detection · intracellular trafficking · ligand–receptor recognition

The unique physical properties of metal-based colloidal nanoparticles, including optical, magnetic, and electronic, have attracted broad interest among scientists from biomedicine-related disciplines in view of their potential application in diagnosis and therapy of malignant diseases.[1–3] However, in order to become suitable for utilization in a biological environment, metal nanoparticles need to be enveloped by a (bio)organic coating.[4,5] The interaction of the resulting hybrid nanoparticles with biomolecules, cells, and tissues represents a key feature for their use in biomedicine. Hence, gathering hybrid nanoparticles together in correspondence to an abnormal lesion results in a localized signal amplification which, in principle, makes it possible to detect even very small size malignancies.[6,7] For example, the accumulation of iron oxide nanoparticles in tumor tissues can be favorable to enhance the contrast in magnetic resonance imaging (MRI) or to optimize the delivery of drugs to cancer cells.[8,9]

Among the various kinds of tumors, breast cancer represents a target of primary interest, both from a diagnostic and from a therapeutic point of view,[10] as it is the fifth most common cause of cancer death worldwide and the most frequent and persistent

malignant cancer in females. At present, one of the main issues in the treatment of breast cancer is the identification of possible metastatic infiltrations at the axillary nodes. The current methods to detect metastases at nodal level require the surgical dissection of the sentinel lymph node, which, however, does not provide a preparatory diagnosis.[11] In this context, the development of innovative target-specific probes able to perform a noninvasive identification of lymph node metastases by MRI represents a primary challenge.[12] For this reason, different strategies aimed to optimize breast cancer diagnosis *in vivo* by the development of multifunctional hybrid organic/inorganic nanomaterials have been proposed,[13,14] and some *in vivo* studies have demonstrated the potential of targeted iron oxide nanoparticles as local enhancers of MRI contrast, especially for metastatic lymph node detection.[15,16] The "human epidermal growth factor receptor 2" (HER2), overexpressed as a transmembrane receptor in 25−30% of human mammary carcinomas, represents a good biomarker for tumor detection.[17] The rationale of taking HER2 as an election molecular target for the identification of lymph nodal metastases resides in the clinical evidence that, while a low level of expression is present even in cells from healthy tissues, HER2 is completely absent in lymph nodes of nonmetastatic patients.[18]

We have recently designed a versatile molecular nanoconstruct consisting of a superparamagnetic iron oxide core functionalized with the commercial anti-HER2 monoclonal antibody trastuzumab (TZ), exploiting the intermediation of a recombinant low-molecular weight monodomain of protein A. These nanocrystals were demonstrated to be effective in selectively targeting HER2 in MCF7 breast cancer cells both *in vitro*[19] and *in vivo*.[20] Further studies, however, revealed that the direct immobilization of the protein ligands on the nanocrystal surface led to a surface exposure to degradation by aggressive activity of biological agents resulting in a loss of long-term stability in a physiological environment.

Nowadays, many efforts are devoted to design nanosystems, which can be localized at cancer cells for an extended period of time, in order to optimize diagnostic sensitivity and therapeutic efficiency. However, to make a full vision of the problem, a thorough knowledge of the interaction of nanoparticles with the target cells, as well as of their intracellular fate, is necessary. Thus, recent studies were aimed to correlate the physicochemical properties of nanomaterials (*i.e.*, size, shape, and surface charge) with the kinetics of internalization, intracellular localization, exocytosis, and rate of degradation in target cells.[21−25] Indeed, an investigation of how size, shape, and chemistry of nanoparticles affect their delivery in cancer cells is essential to redesign tracers and drug delivery systems able to accumulate efficiently at the tumor. A recent study describing internalization, trafficking, and metabolism of nanoparticles in cells has disclosed the involvement of different endocytic mechanisms and intracellular pathways.[26] We have already demonstrated that TZ-conjugated magnetic nanoparticles administered to breast-cancer-bearing mice are able to selectively target the implanted MCF7 cells, enhancing MRI contrast of HER2-positive tissues, and then enter such tumor cells by a receptor-mediated internalization mechanism to be eventually degraded by a lysosomal pathway.[20] However, controversial evidence has been provided on the real importance of molecular targeting to improve the localization of nanomaterials at a specific malignant lesion.[27−29] Indeed, while ligand-mediated interaction with a membrane receptor has been established to be the preferred route to enhance selectivity in the nanoparticle interaction with cancer cells, enhanced permeation and retention (EPR) effect has been proposed by several groups to be the preferred route to achieve higher nanoparticle accumulation at the tumor site *in vivo*, which, in contrast, should be favored by nonfunctionalized long-circulating nanoparticles.[30−33] For this reason, new reliable strategies for getting control on positioning of targeting molecules on the surface of multifunctional nanoparticles (MNP) have been developed to shed light on this debate.[5,34−36]

The aim of the present work was to investigate the dependence of targeting efficiency and biodistribution of HER2-directed multifunctional nanoparticles engineered with TZ derivatives on the structural features of the immobilized homing ligands. Specifically, we have developed three different hybrid MNPs consisting of a common nanocolloidal core functionalized (1) with TZ, (2) with a TZ half-chain obtained by mild reduction of disulfide bridges between the IgG heavy chains (HC), and (3) with an anti-HER2 scFv containing a cysteine residue in the loop useful for site-specific immobilization (C-scFv).[37,38] The shared colloidal core exploited in the present work was an iron oxide nanocrystal coated with a highly soluble amphiphilic polymer for which we have preliminary evidence that long-term stability is significantly improved compared with our previous similar nanocomplexes. The resulting three nanoconstructs were exploited to perform *in vitro*, *in vivo*, and *ex vivo* experiments to compare their targeting potential toward a HER2-positive breast cancer murine model. Accurate cellular and subcellular analyses were also performed to characterize the interaction of the nanoconstructs with cancer cells.

RESULTS

Synthesis of Targeted Nanoparticles. Highly uniform hydrophobic iron oxide nanocrystals (8.2 ± 1.1 nm by TEM) were synthesized by solvothermal decomposition from iron oleate complex in a solution of octadecene in the presence of oleic acid as capping agent (MNC, Figure 1A).[39] MNCs were suspended in chloroform and transferred to
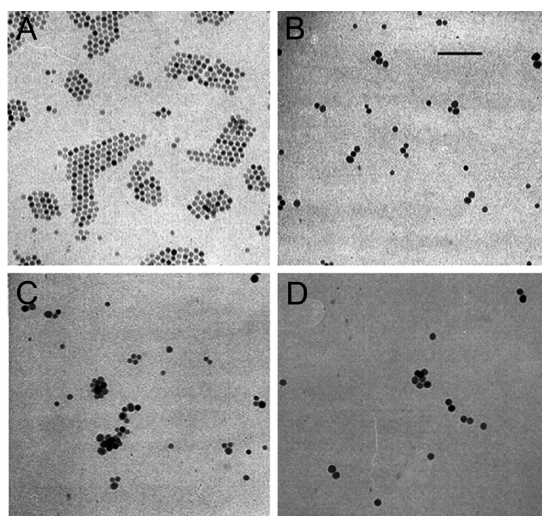
Figure 1. Transmission electron microscopy (TEM) images of (A) MNC, (B) MNP-TZ, (C) MNP-HC, and (D) MNP-scFv. Scale bar: 100 nm.

a water phase after coevaporating with a 0.5 M solution of an amphiphilic polymer (PMA)[40] and resuspending the homogeneous mixture in sodium borate buffer, pH 12. The use of this polymer proved excellent in affording colloidal stability to small nanoparticles even after multiple protein conjugations, which is usually difficult to achieve.[41] The resulting highly water-soluble MNC@PMAs were modified by condensation with 2,20-(ethylenedioxy)bis(ethylamine) (EDBE) and further functionalized with N-succinimidyl-3-[2-pyridyldithio]-propionate (SPDP), giving the common building block for all three nanoconstructs. The resulting thiol-reactive PDP functionalities were exploited for the conjugation of the molecular targeting agent with three different approaches using three different species, namely, TZ, HC, and scFv (Scheme 1).

The first approach, following the immobilization strategy described in a previous report,[19] was based on the use of a recombinant Cys_3-ended single-domain variant of protein A (spaBC3), capable of capturing human IgG molecules via strong binding with their Fc fragment. SpaBC3 allowed for the tight immobilization of TZ in the optimal orientation for binding to HER2, leading to MNP-TZ (Figure 1B). The second approach exploited the thiol groups derived from the rupture of disulfide bonds bridging the two half-chains of the antibody, obtained by pretreatment with the reductive agent MEA (MNP-HC, Figure 1C). In the last approach, the thiol-reactive nanoparticles were reacted with a cys-engineered scFv antibody fragment (C-scFv) cloned and produced in our laboratory, resulting in MNP-scFv (Figure 1D).[38] To improve the conjugation efficiency, C-scFv was pretreated with 1 mM dithiothreitol (DTT) in order to prevent the scFv dimer formation due to the presence of a free cysteine in the peptide sequence.

In all of these approaches, the functionalized MNPs have been saturated with PEG molecules, which act as colloidal stabilizers and reduce nonspecific capture by the reticuloendothelial system. The hydrodynamic size of nanoconstructs was 76.3 ± 9.1 nm (MNP-TZ), 48.7 ± 1.0 nm (MNP-HC), and 53.6 ± 4.4 nm (MNP-scFv), as measured by dynamic light scattering (DLS), while the zeta-potential was −27.2 ± 5.7, −44.5 ± 9.9, and −51.1 ± 2.4 mV, respectively. Representative size distribution curves are reported in Figure S1 in the Supporting Information.

In Vitro **Assays.** The binding capability of MNP-TZ, MNP-HC, and MNP-scFv was first evaluated by flow cytometry. MNP-TZ, MNP-HC, and MNP-scFv ($20 \mu g\,mL^{-1}$) labeled with fluorescein isothiocyanate (FITC) were incubated 1 h with HER2-positive MCF7 cells. As a negative control of binding specificity used to set up the positive region, we have incubated each set of nanoparticles with HER2-negative MDA cells. Flow cytometry evidenced a right-shift of fluorescence signal compared to the negative control, which demonstrated the capability of MNP-TZ, MNP-HC, and MNP-scFv of specifically recognizing HER2 receptors on the MCF7 cell surface (Figure 2A). Percentage values of cells in the positive region for each kind of nanoparticle (Figure 2B) suggest that no significant differences occurred in binding capability between MNP-TZ, MNP-HC, and MNP-scFv. Moreover, nonspecific uptake was basically negligible.

To validate flow cytometry data, the specificity of binding of MNP-TZ, MNP-HC, and MNP-scFv with HER2 receptors was assessed by confocal laser scanning microscopy (Figure 2C). MCF7 cells and, as a negative control, MDA cells were incubated 1 h at 37 °C in the presence of MNP-TZ, MNP-HC, and MNP-scFv ($100 \mu g\,mL^{-1}$). As expected, all three nanoconstructs colocalized with the HER2-positive cell membrane, confirming that they were actually able to specifically target the receptor. However, MNP-HC and MNP-scFv readily distributed inside the cell and even close to the nucleus, whereas MNP-TZ was found only in the proximity of the cell surface.

Cell toxicity of all MNP was then assessed (see Supporting Information Figure S2). We first evaluated the effects of MNP-TZ, MNP-HC, and MNP-scFv on cell viability through an MTT assay. After 24 h of incubation with nanoparticles (20 and $100 \mu g\,mL^{-1}$ for each set), MCF7 proliferation was not significantly affected compared to untreated samples. After 48 h, however, we observed a reduction in the proliferation rate of treated samples that is probably attributable to a loss of nanoparticle stability in culture medium at these concentrations. Cell death of MCF7 cells exposed to MNP-TZ, MNP-HC, and MNP-scFv was also investigated. No significant differences were observed between untreated and MNP-treated cells in terms of toxicity at 20 and $100 \mu g\,mL^{-1}$ after 4 and 24 h of exposure. Taken together, these results indicated a good profile of safety for all three nanoconstructs in cell cultures.

In Vivo **Targeting of a HER2-Positive Tumor.** The efficiency of MNP-TZ, MNP-HC, and MNP-scFv in targeting *in vivo*
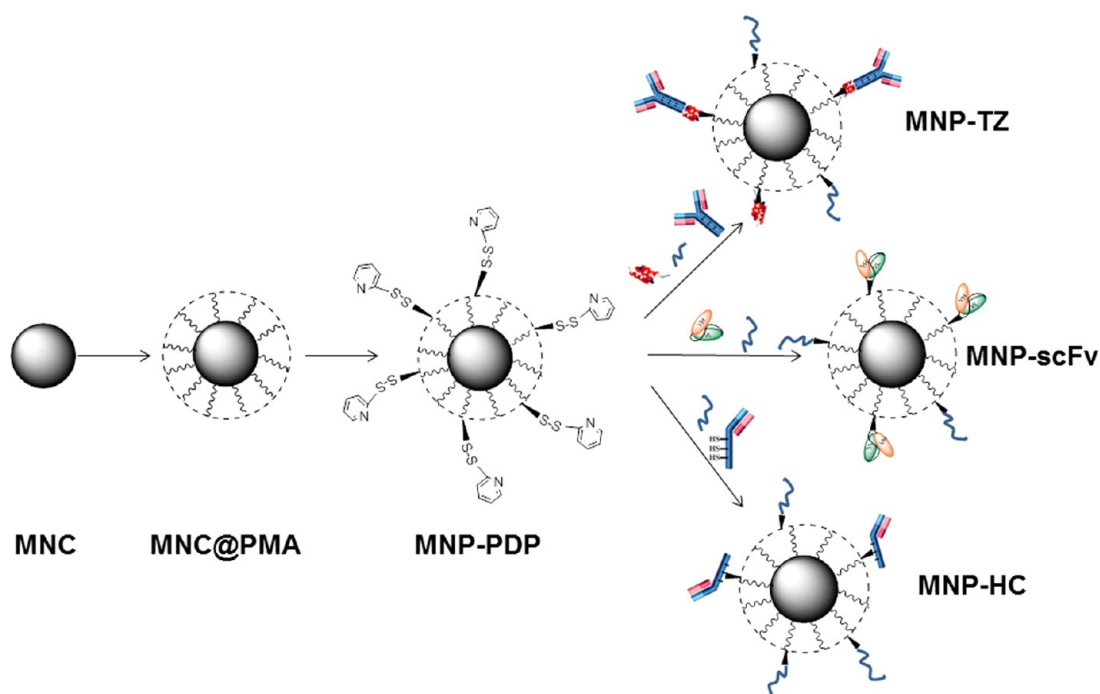
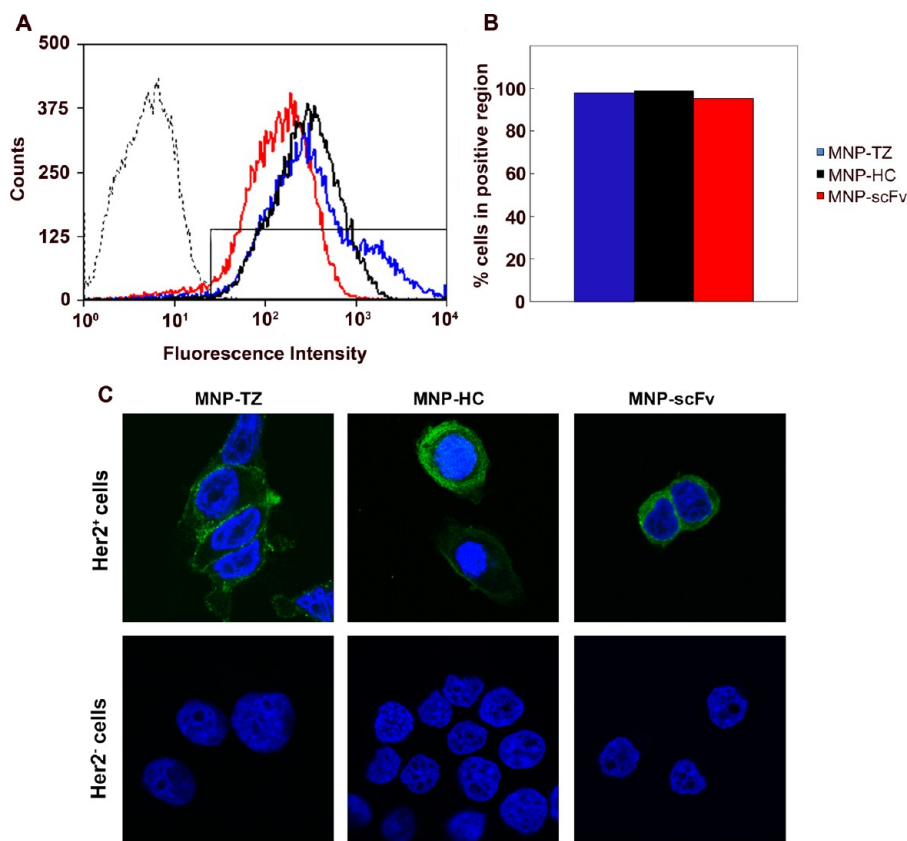Scheme 1. Step sequence for the preparation of MNP-TZ, -HC, and -scFv.

Figure 2. Assessment of HER2 targeting efficacy. (A) Flow cytometry. MCF7 cells were incubated 1 h at 37 °C with MNP-TZ (blue line), MNP-HC (black line), or MNP-scFv (red line). As negative control, MCF7 untreated cells were reported as black and dashed lines. MDA cells incubated with MNP-TZ, MNP-HC, and MNP-scFv were used to set the positive region. (B) Percentage of cells in the positive region. (C) Confocal microscopy images of MCF7 or MDA (negative control) cells, incubated for 1 h at 37 °C with FITC-labeled MNP-TZ, MNP-HC, or MNP-scFv. Nuclei were stained with DAPI. Scale bar: 10 μm.

HER2-positive tumors has been compared. Balb/c nude mice bearing a subcutaneous breast cancer (0.8 cm size) grown by local injection of HER2-positive MCF7 cells were treated with nanoparticles labeled with AlexaFluor 660 (AF660). MNP-TZ, MNP-HC, or MNP-scFv (5 μg g^{-1} body weight) nanoparticles were injected in mice by the tail vein, and their localization in MCF7 tumor was monitored 5 and 48 h after injection by an IVIS Lumina II imaging system. Epifluorescence (Epf) images of anesthetized supine mice (Figure 3A) indicated that all three nanoconstructs were able to target the HER2-positive tumors at 5 h (I, III, and V). However, after 48 h, the signal intensity in the tumor exposed to MNP-TZ remarkably decreased (II). In contrast, a strong increase in fluorescence intensity was observed in MNP-HC-treated mice (IV), while no significant differences were evident in mice treated with MNP-scFv (VI) compared to those monitored at 5 h. *Ex vivo* analysis of tumor fluorescence was then performed (Figure S3). As the injected solution of MNP-TZ, MNP-HC, and MNP-scFv showed a significant difference in intrinsic fluorescence intensity (*i.e.*, the relative fluorescence of MNP-TZ and MNP-scFv appeared lower compared with the HC nanoconjugate due to the restricted number of labeled antibodies on the nanoparticle surface or to the small number of lysine residues available in the peptide sequence for dye labeling, respectively), we chose to normalize the recorded Epf values and homogenate fluorescence, in order to provide a more appropriate comparison between the three nanocomplexes. The results obtained confirmed a strong decrease over time of MNP-TZ Epf intensity, becoming undetectable after 48 h (Figures 3B and S3), and similarly, a remarkable and significative drop of fluorescence was also observed in tumor homogenates (Figure 3C). The increase over time of MNP-HC Epf detected in living animals was confirmed by *ex vivo* images, as well as the behavior of MNP-scFv, whose signal intensity in the tumor mass did not change from 5 to 48 h after injection (Figure 3B and S3). The relative fluorescence in tumor homogenates was in accordance with Epf results for MNP-HC, while only a slight, although significant, increase in fluorescence intensity was detected in MNP-scFv-treated tumors (Figure 3C). To disclose possible differences in uptake efficiency and/or lysosomal degradation of these nanoparticle models, the interaction of injected nanoparticles with tumor cells and their intracellular fate was investigated at the cellular and subcellular level from tumor extracts.

Fate of Nanoparticles in Cells from Tumor Extracts. The internalization of MNP-TZ, MNP-HC, and MNP-scFv and their fate in cancer cells were disclosed by confocal microscopy and ultrastructural investigations of TEM graphs performed on samples of tumors isolated at 5 and 48 h post-i.v. injection. Figure 4, reporting high-magnification images of tumor cells obtained from confocal microscopy performed on sample cryosections,
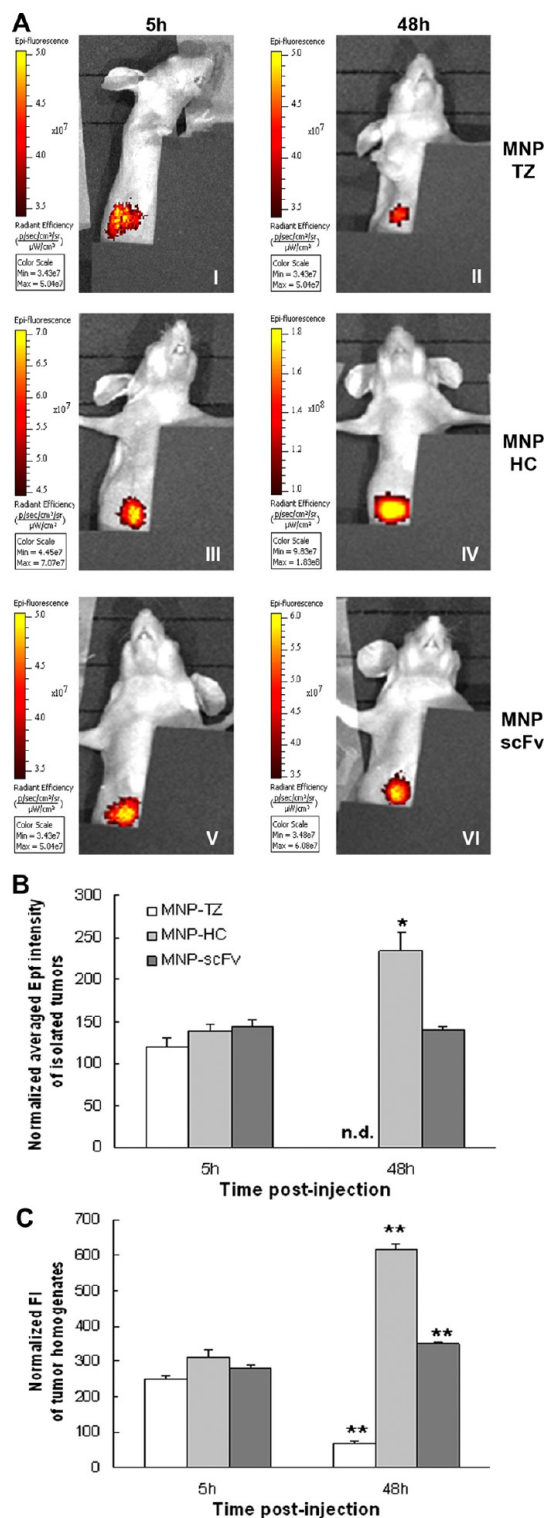

Figure 3. (A) Epifluorescence (Epf) images of mice bearing MCF7 xenografts, acquired 5 or 48 h after exposure to MNP-TZ (I,II), MNP-HC (III,IV), MNP-scFv (V,VI), labeled with AF660. (B) Averaged epifluorescence intensity of the isolated tumors. (C) Fluorescence intensity (FI) of tumor homogenates. Epf and FI values have been normalized on fluorescence intensity of injected solution in order to take into account the differences in intrinsic fluorescence emission for each nanocomplex. Mean $\pm$ SE of three different samples for each experimental condition. *P < 0.01 and **P < 0.001 *vs* 5 h (Student's *t* test).
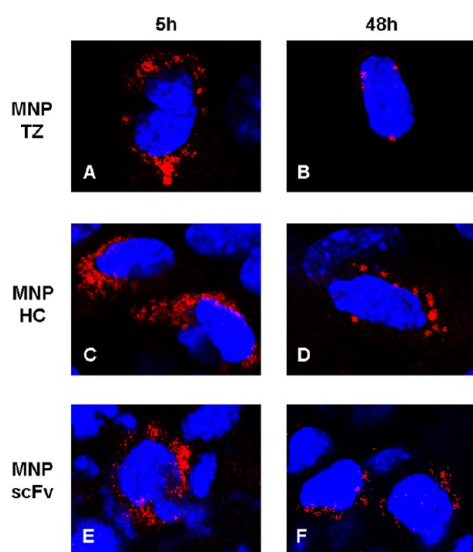
Figure 4. Confocal laser scanning micrographs (single optical sections) of cryosections obtained from MCF7 tumors at 5 and 48 h postinjection of MNP-TZ (A,B), MNP-HC (C,D), or MNP-scFv (E,F) labeled with AF660, and then counterstained with DAPI for nuclei detection. The confocal images of nanocrystals (red) have been overlaid on the corresponding images reporting nuclei (blue). Scale bar: 10 μm.

Figure 5. TEM images of MCF7 tumors isolated at 5 and 48 h postinjection of MNP-TZ (A–D), MNP-HC (E–H), or MNP-scFv (I–N). To the right of each single figure, the corresponding higher magnification image is reported. Nanoparticles and cell membranes are evidenced by small and big arrows, respectively. Scale bars: 100 nm.

showed that at 5 h labeled MNP-TZ appeared mainly localized at the cell periphery (A), while fluorescence of MNP-HC (C) and MNP-scFv (E) spread out uniformly inside the cell, suggesting that the smaller and more stable MNP-HC and MNP-scFv were endocytosed by tumor cells faster than MNP-TZ. This hypothesis, formulated by *in vitro* (Figure 2C) and *ex vivo* (Figure 4) confocal observation, was supported by TEM images (Figure 5). All three nanoparticle models came into contact with the plasma membrane of tumor cells at 5 h (Figure 5A,E,I), but they were internalized with different rates. MNP-TZs were identified only in vesicles displaced under the plasma membrane and feasibly belonging to the early endosomal network (Figure 5B), while MNP-HC and MNP-scFv were observed in endosomes located deep inside the cytoplasm (Figure 5F,L). Optical images show that, after 48 h, MNP-TZ fluorescence was limited to a few perinuclear spots (Figure 4B), and the total staining intensity appeared strongly reduced. This result was in line with data obtained by IVIS and spectrofluorimetric assays and suggested that MNP-TZs were internalized by tumor cells and immediately directed to the lysosomal pathway to be rapidly degraded in the organic component. TEM analyses furnished the conclusive proof, revealing the presence of MNP-TZ at 48 h in lysosomes (Figure 5C,D). Confocal analyses of MNP-HC cryosections (Figure 4D) indicated a perinuclear distribution of the fluorescence analogue to MNP-TZ at 48 h. Nevertheless, the number and the fluorescence intensity of MNP-HC spots were higher than those of the MNP-TZ samples. TEM images provided evidence that MNP-HC did not distribute in lysosomes, but they were still detectable in endosomes
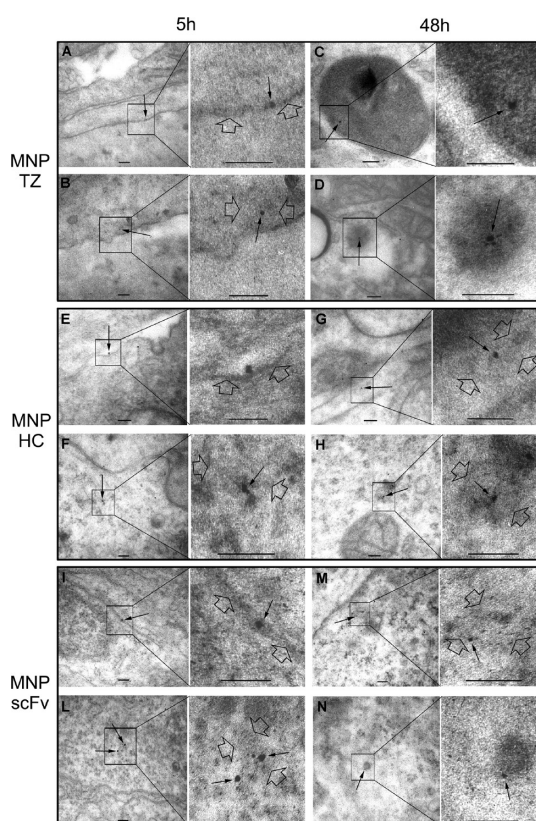
deep inside the cytoplasm, feasibly resembling late endosomes (Figure 5G,H).

After 48 h of exposure to MNP-scFv, confocal images of tumor cryosections showed the same perinuclear fluorescence observed for MNP-HC, even though the resolution of MNP-scFv spots appeared underestimated by the lower signal intensity of these nanoparticles (Figure 4F). TEM observations revealed that MNP-scFv distributed both in endosomes (Figure 5M) and in lysosomes (Figure 5N), suggesting a degradation rate intermediate between MNP-TZ and MNP-HC.

Biodistribution. Biodistribution of injected MNP-TZ, MNP-HC, and MNP-scFv in mice was determined by analyzing model organs with the same methods described above for extracted tumors. The overall results, reported in Supporting Information Figure S4, indicated that MNP-TZ, MNP-HC, and MNP-scFv mainly accumulated in liver and kidneys, even though only a transitory capture by kidneys looked feasible, in accordance with the size limit allowed for particle excretion by this organ.[42] The Epf decreased in liver and kidneys of treated mice within the first 48 h, suggesting the progressive elimination of all three nanoconstructs, which could be particularly promising for potential clinical application.

Active Targeting Discrimination *in Vivo*. In the light of the remarkably better performance of MNP-HC suggested by the above-mentioned results, we selected this nanoconstruct to evaluate the importance of active molecular recognition in targeting tumor cells *in vivo*. The accumulation of MNP-HC in MCF7 tumor mass in living mice was compared with tumor distribution of the following negative controls: (1) unconjugated PE-Gylated MNP (MNPP) and (2) MNP conjugated with the half-chain of a nonspecific rabbit IgG (MNP-HC(IgG)). For a more appropriate comparison of biodistribution of these three nanoconstructs, nanoparticles were labeled with AF660 directly on the PMA shell (see Supporting Information). Figure 6A confirmed the efficient targeting of MNP-HC toward HER2-positive solid tumors at 5 h postinjection. A reliable Epf signal was also observed in MNPP and MNP-HC(IgG)-treated mice to indicate a nonnegligible EPR effect at 5 h after treatment. Nevertheless, while fluorescence intensity of the tumor exposed to MNP-HC increased after 48 h, a drop of fluorescence was observed for MNPP and MNP-HC(IgG). A determination of fluorescence intensity was then performed in isolated tumors. Averaged Epf and homogenate fluorescence values, normalized on the fluorescence intensity of injected solution (see Materials and Methods), were reported in Figure 6B,C, respectively. In accordance with the results of Figure 3 and in line with *in vivo* images (Figure 6A), a significant increase of fluorescence intensity with time was observed in the tumors exposed to MNP-HC, while no significant differences were evident in mice treated with MNPP or MNP-HC(IgG). Figure 6B,C also showed a strongly reduced distribution of MNPP in tumors, whose fluorescence values were 10−30-fold lower than that observed with the antibody-conjugated nanoparticles ready after 5 h. Epf-related biodistribution of the three nanoconstructs in some model organs confirmed the preference of MNP in liver and kidneys, regardless of antibody conjugation (Figure S5). Furthermore, we observed an Epf intensity in the organs of MNPP-treated mice 15-fold lower than that of MNP-HC and MNP-HC(IgG), in agreement with tumor distribution values.

DISCUSSION

At present, diagnosis of axillary localization of breast cancer metastases is based on invasive detection methods, which involve the sentinel lymph node biopsy. In this context, one of the most significant goals is represented by the identification of new target-specific contrast agents able to optimize breast cancer diagnosis and metastatic localization by MRI. The present paper describes the potential of multifunctional nanoparticles bioengineered with variants of anti-HER2 monoclonal antibody to target HER2-positive tumors and accumulate in cancer cells. To this aim, three PEGylated magnetofluorescent nanoparticles have been synthesized by functionalizing the
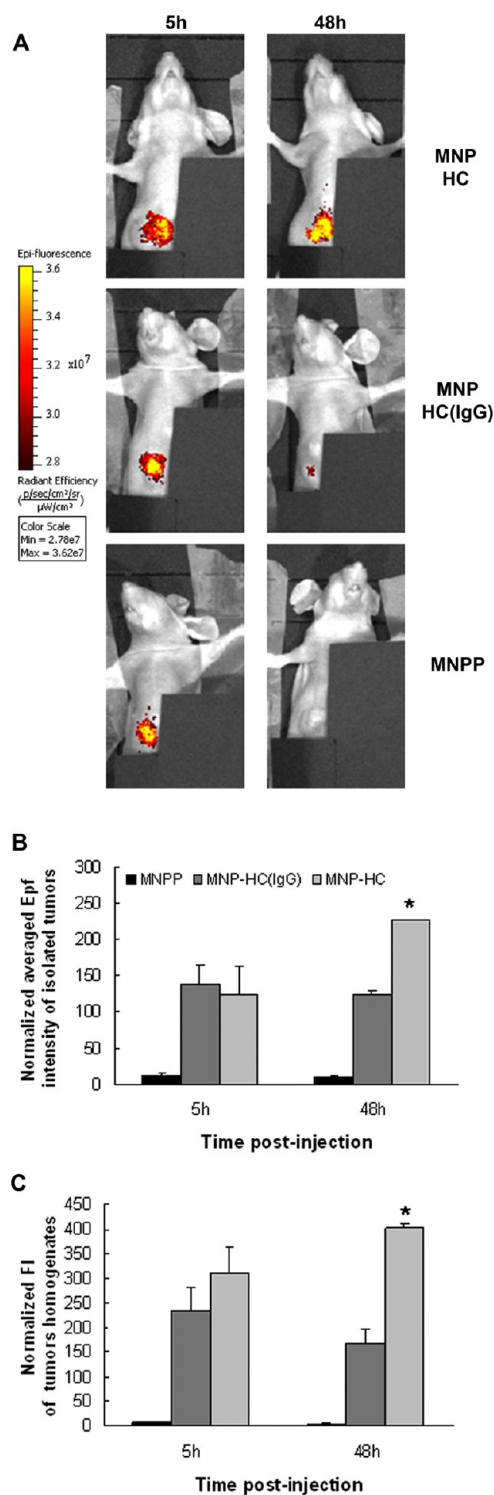

Figure 6. (A) Epifluorescence (Epf) images of mice bearing MCF7 xenografts, acquired 5 or 48 h after exposure to MNPP, MNP-HC(IgG), or MNP-HC, labeled with AF660 on the PMA shell. (B) Averaged epifluorescence intensity of the isolated tumors. (C) Fluorescence intensity (FI) of tumor homogenates. Epf and FI values have been normalized on fluorescence intensity of injected solution in order to take into account the differences in intrinsic fluorescence emission for each nanocomplex. Mean $\pm$ SE of three different samples for each experimental condition. *$P < 0.05$ *vs* 5 h (Student's *t* test).

surface with trastuzumab, or with the antibody variants HC and scFv, in order to optimize the targeting efficiency. All of these nanoparticles proved to be highly effective in selectively targeting HER2-positive breast cancer cells *in vitro*, but their behavior *in vivo*, assessed by fluorescence analyses and transmission electron microscopy, revealed several differences. The results obtained with the fluorescent nanoconstructs indicated that all three variants were able to target HER2-positive MCF7 breast cancer cells *in vitro* (Figure 2), *in vivo*, and *ex vivo* (Figures 3 and S3). Starting from the assumption that the ideal candidate for cancer diagnosis should be a nanosystem able to localize itself at cancer cells for an extended period of time, we decided to investigate the behavior of the three nanoconstructs at 5 and 48 h postinjection in MCF7 tumor-bearing mice. We found that MNP-scFv represented a more efficient probe compared to MNP-TZ because its Epf in the tumor mass did not decrease over time, as conversely occurred with the whole antibody. Nevertheless, the most significant result has been obtained with MNP-HC, whose Epf in the 48 h xenograft was even higher than that recorded after 5 h. The trend over time of tumor fluorescence suggested a possible different behavior for the three nanoprobes in cancer cells, especially referred to a different timing of interaction and incorporation of nanoparticles. In fact, while MNP-TZ followed the same mechanism of entry and fate in cancer cells previously described for similar TZ-engineered nanoarchitectures,[20] involving a receptor-mediated internalization followed by degradation of the organic shell by a lysosomal pathway, a comparable degradative process did not seem to affect MNP-HC and MNP-scFv within the first 48 h from injection.

To better disclose the subcellular activity of MNP-TZ, MNP-HC, and MNP-scFv, a comparative analysis of internalization, trafficking, and metabolism in MCF7 cells of the different nanoparticles was performed by confocal and electron microscopy. The overall results demonstrated that MNP-HC and MNP-scFv were endocytosed by MCF7 cells faster than MNP-TZ (Figures 2C, 4, and 5), in line with previous findings describing a strict relationship between the size of protein-coated nanoparticles and the rate of uptake by a receptor-mediated mechanism, referred to as the so-called "wrapping time".[21,43] According to this theory, single spherical nanoparticles smaller than 50 nm diameter should not produce enough free energy to be endocytosed by the tumor cell and more clustered nanoparticles are necessary to trigger the wrapping process. Conversely, for nanoparticles larger than 50 nm, the wrapping time is inversely proportional to the size. More receptors are taken up during the binding process with a consequent effect on the kinetic of recruitment on the cell membrane. The hydrodynamic diameter of MNP-HC and MNP-scFv was around 50 nm, while the dispersed MNP-TZ had

a diameter of about 80 nm, although we found that the low stability of MNP-TZ originated aggregates in serum of size up to 310 nm. The presence of MNP-TZ aggregates could feasibly justify the slow internalization of MNP-TZ in MCF7 cells compared to MNP-HC and MNP-scFv.

Once internalized, all three nanoparticles were directed to the endosome–lysosome pathway, but significant differences were observed also in the trafficking and degradation timing (Figure 4). TEM observation clearly revealed that while MNP-TZ, endocytosed by cell membrane at a slower rate, quickly addressed the lysosomal system to be immediately degraded, MNP-scFv and MNP-HC remained within endosome-like vesicles for an extended period of time. More specifically, at 48 h postinjection, MNP-scFv compared both in endosomes and in lysosomes, while no lysosomes containing MNP-HC have been detected (Figure 5). We thus postulated also that MNP-HC would be finally driven to the lysosomal pathway, although at a much slower rate. The reason behind the different rate in MNP-TZ, MNP-HC, and MNP-scFv intracellular trafficking remains at least partially unclear. While the low MNP-TZ stability can feasibly affect the intracellular fate of this nanoconstruct, the differences between MNP-HC and MNP-scFv trafficking are less obvious because the variation in size is not enough to justify such an influence. We speculated that the behavior of these nanoconstructs could be related to the different interactions of the two antibody variants with the target cell, accounting for a receptor-mediated active targeting.

Active targeting contribution to the distribution of nanoparticles in solid breast cancer has been determined *in vivo*, by comparing the accumulation in the tumor mass of MNP-HC and nonspecifically targeted nanoparticles. Indeed, the EPR effect, often responsible for the high distribution of administered drugs in tumor area,[44] could be the cause of the strong accumulation of biofunctionalized MNP in mice xenografts (Figures 3 and S3). We demonstrated that the presence of the HER2-directed ligands on the MNP surface increases the overall concentration of nanoparticles in solid tumors within the first 48 h post-treatment, while unconjugated MNP or nanoparticles engineered with the nonspecific IgG ligand do not accumulate in tumors for such a long time (Figure 6). The very low amount of MNPP observed in tumor and organs (Figures 6B,C and S5) suggested that nonfunctionalized nanoparticles were rapidly excreted by the organism, in agreement with their small size.

CONCLUSION

Our study demonstrates the importance of evaluating *in vivo* the targeting efficiency of nanoconstructs bearing homing ligands, even though they manifest similar cell binding capability in culture. In summary, the results of this study suggest that (1) the aggregation state of nanoparticle formulation is crucial for their final destination once they reach the cellular target;

(2) the interaction of antibody-functionalized MNP with HER2-positive cancer cells, which affects their intracellular fate, is at least partly dependent on the affinity of the receptor for the peptide ligand; (3) although EPR effect allows short-term accumulation of all nanoparticles of this family irrespective of the presence of targeting ligands, only receptor-specific functionalization affords long-term action in cancer cells *in vivo*; (4) the

longer period of accumulation of MNP-HC in the tumor makes this nanoparticle the ideal candidate for future application in breast cancer diagnosis. Further investigations will be necessary to assess the effects of the nature of different antibody derivatives (*i.e.*, entire IgG, HC, or scFv) on the intracellular fate of MNP and their interference with cell processes with obvious repercussion on biomedical potential of targeted nanoparticles.

MATERIALS AND METHODS

Synthesis of MNP-TZ, MNP-HC, and MNP-scFv. Surfactant-coated Fe_3O_4 nanocrystals (MNCs) were synthesized in organic solvent and transferred to water phase, according to the procedure described in Supporting Information. The resulting core−shell nanoparticles (MNC@PMA) were functionalized in order to obtain the thiol-reactive MNP (MNP-PDP, Scheme 1) and processed for the production of the final constructs.

To obtain trastuzumab-conjugated nanoparticles (MNP-TZ), MNPs were functionalized with an individual B domain of protein A (spaBC3), as described in our previous work.[19] Briefly, MNP-PDP (1 mg) was incubated in the presence of spaBC3 (0.5 mg). The remaining PDP functional groups were saturated with excess PEG$_{500}$-SH. TZ was labeled with AF660 dye (Life Technologies) according to manufacturer's protocol. TZ conjugation on nanoparticles was performed by incubating nanoparticles (1 mg) at room temperature for 2 h in the presence of labeled TZ (0.3 mg). Excess chemicals and biological reagents were removed by dialysis, and the MNP-TZs were collected.

For the production of MNP-HC, AlexaFluor 660-labeled TZ dissolved in EDTA−PBS (1 mg mL^{-1}) was added to the 2-mercaptoethanolamine kit (MEA, Thermo Scientific) and treated according to manufacturer's protocol to reduce the disulfide bridges between the two heavy chains of the IgG, obtaining the half-chain antibody portions. The HCs were immediately added to MNP (1 mg) and incubated at room temperature for 1 h. The remaining PDP functional groups were saturated with excess PEG$_{500}$-SH. Excess chemicals and biological reagents were removed by dialysis, and MNP-HCs were collected.

To synthesize MNP-scFv, MNPs (10 mg) were incubated in the presence of cysteine-modified ScFv molecules (2 mg), obtained by site-directed mutagenesis of scFv800E6,[37] as previously reported.[38] Before incubation with MNP, scFv was labeled with AF660 dye (Life Technologies) according to manufacturer's protocol and treated with 0.1 M DTT. The remaining PDP functional groups were saturated with excess PEG$_{500}$-SH and incubated at room temperature for 1 h. Excess chemicals and biological reagents were removed by dialysis, and MNP-scFv were collected.

Flow Cytometry. MCF7 and MDA-MD-468, cultured as described in Supporting Information, were used as HER2-positive and HER2-negative cellular models, respectively. For the flow cytometry, cells were cultured on a 6-multi-well dish until subconfluence. Then, cells were incubated 1 h at 37 °C in the presence of MNP-TZ, MNP-HC, and MNP-scFv (20 μg mL^{-1}) labeled with FITC. After incubation, cells were washed three times with PBS, and labeled cells were analyzed on a FACS Calibur flow cytometer (Becton Dickinson); 20 000 events were acquired for each analysis after gating on viable cells.

Cell Death and Proliferation Assays. To assess cell death, MCF7s were cultured on a multi-well dish until subconfluence. Cells were then incubated 4 and 24 h at 37 °C in the presence of MNP-TZ, MNP-HC, and MNP-scFv (20 or 100 μg mL^{-1}). After incubation, cells were washed twice with PBS and treated for FACS analysis according to PE Annexin V apoptosis detection kit I manufacturer's protocol (Becton Dickinson Biosciences). Briefly, cells were resuspended in 1× binding buffer and incubated for 15 min in presence of 0.005 mL of Annexin-PE and 0.005 mL of 7-aminoactinomycin D to be then analyzed on FACS within the subsequent 1 h; 20 000 events were acquired for each analysis

after gating on viable cells. Cell death is determined as the populations positive for Annexin V and for 7AAD staining alone and together.

For the proliferation assay, MCF7 cells were cultured on a 96-multi-well dish at a density of 5000 cells cm^{-1} and then incubated with MNP-TZ, MNP-HC, and MNP-scFv (20 or 100 μg mL^{-1}). At the indicated time points, cells were washed with PBS and then incubated for 3 h at 37 °C with 0.1 mL of 3-(4,5-dimethyl-2-thiazolyl)-2,5-diphenyl-2H-tetrazolium bromide (MTT) stock solution previously diluted 1:10 in DMEM medium without phenol red. At the end of the incubation, 0.1 mL of MTT solubilizing solution was added to each well to solubilize the MTT formazan crystals (Sigma-Aldrich). Absorbances were read immediately in a BIORAD microplate reader using a test wavelength of 570 nm and a reference wavelength of 690 nm.

In Vivo and *Ex Vivo* Assays. MCF7 cells were injected in female Balb/c nude mice to obtain a valid breast cancer model (see details in Supporting Information). AF660-labeled nanoparticles (5 μg g^{-1} body weight) were injected in the tail vein of breast cancer bearing mice. Epifluorescence imaging was performed at 5 and 48 h postinjection by placing the animals, anesthetized by i.p. injection of 20 mg mL^{-1} of Avertin, in a IVIS Lumina II imaging system (Calipers Life Sciences) at 37 °C. Images were acquired with a 720 nm emission filter, and excitation was scanned from 570 to 640 nm; mice autofluorescence was removed by spectral unmixing. After *in vivo* acquisitions, mice were sacrificed and dissected tumors and organs (liver, kidneys, spleen, and lungs) were analyzed in the IVIS system, as described above for the whole animals. All Epf values of the isolated tissues were normalized on the Epf obtained by IVIS acquisition of the different nanoparticle solutions in a 96-well plate (×10^3).

Fluorescence intensity of tumor, liver, kidney, spleen, and lung homogenates was also measured. According to the procedure, the isolated tissues were weighed and homogenized with ultraturrax in a homogenization buffer (0.32 M sucrose, 100 mM Hepes, pH 7.4). Protein concentration of the samples was measured using the bicinchonic acid (BCA, Pierce) protein assay, and fluorescence was analyzed in a GloMax multi detection system (Promega). All tissue fluorescence values were normalized on the fluorescence intensity of the different nanoparticle solutions (×10^5).

Confocal Laser Scanning Microscopy. For confocal microscopy observations, MCF7 and MDA cells were cultured on collagene (Sigma-Aldrich) precoated coverglass slides until subconfluence and were incubated 1 h at 37 °C with 100 μg mL^{-1} of MNP-TZ, MNP-HC, and MNP-scFv. Then, cells were washed twice with PBS, fixed for 10 min with 4% paraformaldehyde (Sigma-Aldrich), and treated for 10 min with 0.1 M glycine (Sigma-Aldrich) in PBS. Cells were permeabilized with an incubation of 5 min at room temperature in 0.1% Triton X-100 in PBS. A blocking step was performed for 1 h at room temperature with a solution containing 2% bovine serum albumin (Sigma-Aldrich) and 2% goat serum in PBS. Nuclei were stained with DAPI (4′,6-diamidino-2-phenylindole, Life Technologies) at a 1:10000 dilution in blocking buffer for 20 min at room temperature. Microscopy analysis was performed with a Leica SP2 AOBs microscope confocal system (Leica Microsystems). Images were acquired with 63× magnification oil immersion lenses at 1024 × 1024 pixel resolution.

For the confocal microscopy of cryosections, MCF7 tumors were isolated and fixed in 4% paraformaldehyde solution for 3 h,

washed in PBS, and embedded in OCT (VWR, International) for freezing in liquid nitrogen. Ten micrometer thick tumor cryosections were air-dried at room temperature for 1 h, rinsed with PBS, and, after 5 min of permeabilization at room temperature with 0.1% Triton X-100 in PBS, counterstained with DAPI (diluted 1:1500 in PBS) for 20 min at room temperature. Microscopy analysis of cryosections was performed with a Leica TCS SPE confocal microscope (Leica Microsystems) at Fondazione Filarete, Milano, Italy. Images were acquired with 40× magnification oil immersion lenses at 1.5 zoom and 1024 × 1024 pixel resolution.

Transmission Electron Microscopy (TEM). Small portions of MCF7 tumor samples were fixed in 2.5% glutaraldehyde (Electron Microscopy Sciences) in 0.1 M phosphate buffer, pH 7.2, for 2 h. After one rinse with phosphate buffer, specimens were postfixed in 1.5% osmium tetroxide (Electron Microscopy Sciences) for 2 h, dehydrated by 70, 90, and 100% EtOH, and embedded in epoxy resin (PolyBed 812 Polysciences Inc). Ultrathin sections were examined by means of a transmission electron microscope (Zeiss EM109).

Conflict of Interest: The authors declare no competing financial interest.

Supporting Information Available: In vitro toxicity assays, Epf images of isolated tumors and organs, nanoparticles biodistribution values. This material is available free of charge *via* the Internet at http://pubs.acs.org.

REFERENCES AND NOTES

1. Lee, J. H.; Huh, Y. M.; Jun, Y. W.; Seo, J. W.; Jang, J. T.; Song, H. T.; Kim, S.; Cho, E. J.; Yoon, H. G.; Suh, J. S.; *et al.* Artificially Engineered Magnetic Nanoparticles for Ultra-sensitive Molecular Imaging. *Nat. Med.* **2007**, *13*, 95–99.
2. Park, K.; Lee, S.; Kang, E.; Kim, K.; Choi, K.; Kwon, I. C. New Generation of Multifunctional Nanoparticles for Cancer Imaging and Therapy. *Adv. Funct. Mater.* **2009**, *19*, 1553–1566.
3. Goesmann, H.; Feldmann, C. Nanoparticulate Functional Materials. *Angew. Chem., Int. Ed.* **2010**, *49*, 1362–1395.
4. Haun, J. B.; Devaraj, N. K.; Hilderbrand, S. A.; Lee, H.; Weissleder, R. Bioorthogonal Chemistry Amplifies Nanoparticle Binding and Enhances Signal Detection. *Nat. Nanotechnol.* **2010**, *5*, 660–665.
5. Colombo, M.; Mazzucchelli, S.; Collico, V.; Avvakumova, S.; Pandolfi, L.; Corsi, F.; Porta, F.; Prosperi, D. Protein-Assisted One-Pot Synthesis and Biofunctionalization of Spherical Gold Nanoparticles for Selective Targeting of Cancer Cells. *Angew. Chem., Int. Ed.* **2012**, *51*, 9272–9275.
6. Vaijayanthimala, V.; Cheng, P. Y.; Yeh, S. H.; Liu, K. K.; Hsiao, C. H.; Chao, J. I.; Chang, H. C. The Long-Term Stability and Biocompatibility of Fluorescent Nanodiamond as an *In Vivo* Contrast Agent. *Biomaterials* **2012**, *33*, 7794–7802.
7. Chen, T. J.; Cheng, T. H.; Chen, C. Y.; Hsu, S. C.; Cheng, T. L.; Liu, G. C.; Wang, Y. M. Targeted Herceptin-Dextran Iron Oxide Nanoparticles for Noninvasive Imaging of HER2/Neu Receptors Using MRI. *J. Biol. Inorg. Chem.* **2009**, *14*, 253–260.
8. Colombo, M.; Carregal-Romero, S.; Casula, M. F.; Gutiérrez, L.; Morales, M. P.; Böhm, I. B.; Heverhagen, J. T.; Prosperi, D.; Parak, W. J. Biological Applications of Magnetic Nanoparticles. *Chem. Soc. Rev.* **2012**, *41*, 4306–4334.
9. Prijic, S.; Sersa, G. Magnetic Nanoparticles as Targeted Delivery Systems in Oncology. *Radiol. Oncol.* **2011**, *45*, 1–16.
10. Colombo, M.; Corsi, F.; Foschi, D.; Mazzantini, E.; Mazzucchelli, S.; Morasso, C.; Occhipinti, E.; Polito, L.; Prosperi, D.; Ronchi, S.; *et al.* HER2 Targeting as a Two-Sided Strategy for Breast Cancer Diagnosis and Treatment: Outlook and Recent Implications in Nanomedical Approaches. *Pharmacol. Res.* **2010**, *62*, 150–165.
11. McMasters, K. M.; Tuttle, T. M.; Carlson, D. J.; Brown, C. M.; Noyes, R. D.; Glaser, R. L.; Vennekotter, D. J.; Turk, P. S.; Tate, P. S.; Sardi, A.; *et al.* Sentinel Lymph Node Biopsy for Breast Cancer: A Suitable Alternative to Routine Axillary Dissection in Multi-institutional Practice When Optimal Technique Is Used. *J. Clin. Oncol.* **2000**, *18*, 2560–2566.
12. Weissleder, R.; Pittet, M. J. Imaging in the Era of Molecular Oncology. *Nature* **2008**, *452*, 580–589.
13. Yang, L.; Peng, X. H.; Wang, Y. A.; Wang, X.; Cao, Z.; Ni, C.; Karna, P.; Zhang, X.; Wood, W. C.; Gao, X.; *et al.* Receptor-Targeted Nanoparticles for *In Vivo* Imaging of Breast Cancer. *Clin. Cancer. Res.* **2009**, *15*, 4722–4732.
14. Hathaway, H. J.; Butler, K. S.; Adolphi, N. L.; Lovato, D. M.; Belfon, R.; Fegan, D.; Monson, T. C.; Trujillo, J. E.; Tessier, T. E.; Bryant, H. C.; *et al.* Detection of Breast Cancer Cells Using Targeted Magnetic Nanoparticles and Ultra-sensitive Magnetic Field Sensors. *Breast Cancer Res.* **2011**, *13*, R108–R121.
15. Harisinghani, M. G.; Barentsz, J.; Hahn, P. F.; Deserno, W. M.; Tabatabaei, S.; van de Kaa, C. H.; de la Rosette, J.; Weissleder, R. Noninvasive Detection of Clinically Occult Lymph-Node Metastases in Prostate Cancer. *N. Engl. J. Med.* **2003**, *348*, 2491–2499.
16. Memarsadeghi, M.; Riedl, C. C.; Kaneider, A.; Galid, A.; Rudas, M.; Matzek, W.; Helbich, T. H. Axillary Lymph Node Metastases in Patients with Breast Carcinomas: Assessment with Nonenhanced *versus* USPIO-Enhanced MR Imaging. *Radiology* **2006**, *241*, 367–377.
17. Schechter, A. L.; Stern, D. F. The Neu Oncogene: An Erb-B Related Gene Encoding a 185,000-Mr Tumor Antigen. *Nature* **1984**, *312*, 513–516.
18. Strien, L.; Leidenius, M.; von Smitten, K.; Heikkilä, P. Concordance between HER-2 and Steroid Hormone Receptor Expression between Primary Breast Cancer, Sentinel Node Metastases, and Isolated Tumor Cells. *Pathol. Res. Pract.* **2010**, *206*, 253–258.
19. Mazzucchelli, S.; Colombo, M.; De Palma, C.; Salvadè, A.; Verderio, P.; Coghi, M. D.; Clementi, E.; Tortora, P.; Corsi, F.; Prosperi, D. Single-Domain Protein A-Engineered Magnetic Nanoparticles: Toward a Universal Strategy to Site-Specific Labeling of Antibodies for Targeted Detection of Tumor Cells. *ACS Nano* **2010**, *4*, 5693–5702.
20. Corsi, F.; Fiandra, L.; De Palma, C.; Colombo, M.; Mazzucchelli, S.; Verderio, P.; Allevi, R.; Tosoni, A.; Nebuloni, M.; Clementi, E.; *et al.* HER2 Expression in Breast Cancer Cells Is Downregulated upon Active Targeting by Antibody-Engineered Multifunctional Nanoparticles in Mice. *ACS Nano* **2011**, *5*, 6383–6393.
21. Chithrani, B. D.; Warren, C. W. C. Elucidating the Mechanism of Cellular Uptake and Removal of Protein-Coated Gold Nanoparticles of Different Sizes and Shapes. *Nano Lett.* **2007**, *7*, 1542–1550.
22. Schwiger, C.; Hartmann, R.; Zhang, F.; Parak, W. J.; Kissel, T. H.; Rivera-Gil, P. Quantification of the Internalization Patterns of Superparamagnetic Iron Oxide Nanoparticles with Opposite Charge. *J. Nanobiotechnol.* **2012**, *10*, 28–39.
23. Albanese, A.; Tang, P. S.; Chan, W. C. W. The Effect of Nanoparticle Size, Shape and Surface Chemistry on Biological Systems. *Annu. Rev. Biomed. Eng.* **2012**, *14*, 1–16.
24. Bae, Y. M.; Park, Y. I.; Nam, S. H.; Kim, J. H.; Lee, K.; Kim, H. M.; Yoo, B.; Choi, J. S.; Lee, K. T.; Hyeon, T.; *et al.* Endocytosis, Intracellular Transport, and Exocytosis of Lanthanide-Doped Upconverting Nanoparticles in Single Living Cells. *Biomaterials* **2012**, *33*, 9080–9086.
25. Huhn, D.; Kantner, K.; Geidel, C.; Brandholt, S.; De Cock, I.; Soenen, S. J.; Rivera Gil, P.; Montenegro, J. M.; Braeckmans, K.; Müllen, K.; *et al.* Polymer-Coated Nanoparticles Interacting with Proteins and Cells: Focusing on the Sign of the Net Charge. *ACS Nano* **2013**, *7*, 3253–3263.
26. Iversen, T. G.; Skotland, T.; Sandvig, K. Endocytosis and Intracellular Transport of Nanoparticles: Present Knowledge and Need for Future Studies. *Nano Today* **2011**, *6*, 176–185.
27. Tasciotti, E.; Liu, X.; Bhavane, R.; Plant, K.; Leonard, A. D.; Price, B. K.; Cheng, M. M.-C.; Decuzzi, P.; Tour, J. M.; Robertson, F.; *et al.* Mesoporous Silicon Particles as a Multistage Delivery System for Imaging and Therapeutic Applications. *Nat. Nanotechnol.* **2008**, *3*, 251–157.

28. Ruoslahti, E.; Bhatia, S. N.; Sailor, M. J. Targeting of Drugs and Nanoparticles to Tumors. *J. Cell Biol.* **2010**, *188*, 759–768.

29. Lu, W.; Xiong, C.; Zhang, R.; Shi, L.; Huang, M.; Zhang, G.; Song, S.; Huang, Q.; Liu, G.-y.; Li, C. Receptor-Mediated Transcytosis: A Mechanism for Active Extravascular Transport of Nanoparticles in Solid Tumors. *J. Controlled Release* **2011**, *161*, 959–966.

30. Huo, S.; Ma, H.; Huang, K.; Liu, J.; Wei, T.; Jin, S.; Zhang, J.; He, S.; Liang, X.-J. Superior Penetration and Retention Behavior of 50 nm Gold Nanoparticles in Tumors. *Cancer Res.* **2013**, *73*, 319–330.

31. Wong, C.; Stylianopoulos, T.; Cui, J.; Martin, J.; Chauhan, V. P.; Jiang, W.; Popović, Z.; Jain, R. K.; Bawendi, M. G.; Fukumura, D. Multistage Nanoparticle Delivery System for Deep Penetration into Tumor Tissue. *Proc. Natl. Acad. Sci. U.S.A.* **2011**, *108*, 2426–2431.

32. Wang, M.; Thanou, M. Towards Clinical Applications of Nanoscale Medicines. *Pharmacol. Res.* **2010**, *62*, 90–99.

33. Blanco, E.; Hsiao, A.; Ruiz-Esparza, G. U.; Landry, M. G.; Meric-Bernstam, F.; Ferrari, M. Molecular-Targeted Nanotherapies in Cancer: Enabling Treatment Specificity. *Mol. Oncol.* **2011**, *5*, 492–503.

34. Simberg, D.; Duza, T.; Park, J. H.; Essler, M.; Pilch, J.; Zhang, L.; Derfus, A. M.; Yang, M.; Hoffman, R. M.; Bhatia, S.; *et al.* Biomimetic Amplification of Nanoparticle Homing to Tumors. *Proc. Natl. Acad. Sci. U.S.A.* **2010**, *104*, 932–936.

35. Colombo, M.; Sommaruga, S.; Mazzucchelli, S.; Polito, L.; Verderio, P.; Galeffi, P.; Corsi, F.; Tortora, P.; Prosperi, D. Back Cover: Protein-Assisted One-Pot Synthesis and Biofunctionalization of Spherical Gold Nanoparticles for Selective Targeting of Cancer Cells. *Angew. Chem., Int. Ed.* **2012**, *51*, 496–499.

36. Mazzucchelli, S.; Colombo, M.; Verderio, P.; Rozek, E.; Andreata, F.; Galbiati, E.; Tortora, P.; Corsi, F.; Prosperi, D. Orientation-Controlled Conjugation of Haloalkane Dehalogenase Fused Homing Peptides to Multifunctional Nanoparticles for the Specific Recognition of Cancer Cells. *Angew. Chem., Int. Ed.* **2013**, *52*, 3121–3125.

37. Sommaruga, S.; Lombardi, A.; Salvadè, A.; Mazzucchelli, S.; Corsi, F.; Galeffi, P.; Tortora, P.; Prosperi, D. Highly Efficient Production of Anti-HER2 scFv Antibody Variant for Targeting Breast Cancer Cells. *Appl. Microbiol. Biotechnol.* **2011**, *91*, 613–621.

38. Mazzucchelli, S.; Sommaruga, S.; O'Donnell, M.; Galeffi, P.; Tortora, P.; Prosperi, D.; Colombo, M. Dependence of Nanoparticle-Cell Recognition Efficiency from Surface Orientation of scFv Targeting Ligands. *Biomater. Sci.* **2013**, *1*, 728–735.

39. Park, J.; An, K.; Hwang, Y.; Park, J. G.; Noh, H. J.; Kim, J. Y.; Park, J. H.; Hwang, N. M.; Hyeon, T. Ultra-Large-Scale Syntheses of Monodisperse Nanocrystals. *Nat. Mater.* **2004**, *3*, 891–895.

40. Lin, C. A. J.; Sperling, R. A.; Li, J. K.; Yang, T. Y.; Li, P. Y.; Zanella, M.; Chang, W. H.; Parak, W. J. Design of an Amphiphilic Polymer for Nanoparticle Coating and Functionalization. *Small* **2008**, *4*, 334–341.

41. Colombo, M.; Mazzucchelli, S.; Montenegro, J. M.; Galbiati, E.; Corsi, F.; Parak, W. J.; Prosperi, D. Protein Oriented Ligation on Nanoparticles Exploiting O6-Alkylguanine-DNA Transferase (SNAP) Genetically Encoded Fusion. *Small* **2012**, *8*, 1492–1497.

42. Choi, H. S.; Preeti Misra, W. L.; Tanaka, E.; Zimmer, J. P.; Ipe, B. I.; Bawendi, M. G.; Frangioni, J. V. Renal Clearance of Nanoparticles. *Nat. Biotechnol.* **2007**, *25*, 1165–1170.

43. Gao, H.; Shi, W.; Freund, L. B. Mechanics of Receptor-Mediated Endocytosis. *Proc. Natl. Acad. Sci. U.S.A.* **2005**, *102*, 9469–9474.

44. Torchilin, V. Tumor Delivery of Macromolecular Drugs Based on the EPR Effect. *Adv. Drug Delivery Rev.* **2011**, *63*, 131–135.